A numerical source of small-scale number-density fluctuations in Eulerian–Lagrangian simulations of multiphase flows

Y. Ling, A. Haselbacher, S. Balachandar *

Department of Mechanical and Aerospace Engineering, University of Florida, Gainesville, FL 32611, United States

A R T I C L E   I N F O

A B S T R A C T

Eulerian–Lagrangian simulations of multiphase flow are known to suffer from two errors that can introduce small-scale fluctuations in the number-density of the dispersed phase. These errors can be reduced by increasing the number of particles in the simulation. Here, we present results to demonstrate that a third error exists that can also generate small-scale number-density fluctuations. In contrast to the two known errors, this error cannot be lowered by increasing the number of particles. Analysis shows that this error is caused by spatial variation at the subgrid scale in the interpolation error of the fluid velocity to the particle location. If the particle velocity divergence is zero, the particle concentration error remains at the subgrid scale. However, if particles preferentially accumulate either due to their inertia or due to divergence of the underlying fluid-velocity field, this error manifests as number-density fluctuations on the grid scale. The only mechanism of reducing these errors is through higher-order accurate interpolation. By studying two model problems, estimates for the errors are derived. These estimates are shown to be quite accurate for simulations of shock and expansion waves interacting with particles.

1. Introduction

In Eulerian–Lagrangian simulations of multiphase flows, the carrier (fluid) phase is evolved in the Eulerian framework and the dispersed (fluid or solid) phase is treated by the Lagrangian framework. In the Eulerian approach, conservation equations are solved for the mass, momentum, and energy per unit volume on a fixed grid. In the Lagrangian approach, equations are solved for the position, mass, momentum, and energy of material points that move through the fixed Eulerian grid. (For brevity, we will consider the dispersed phase to be solid and hence refer to the material points as particles. The issues discussed in this article apply equally to bubbles and droplets, however.)

In the Lagrangian equations, quantities such as the undisturbed fluid velocity, fluid acceleration, and fluid temperature are needed at the particle location. Because the particles do not, in general, coincide with the locations at which the fluid solution is stored, some form of interpolation is required. (In this article, we assume that the fluid solution is obtained at grid points through a finite-difference method. Therefore, the fluid properties must be interpolated from grid points to the particle locations.) The interpolation is sometimes referred to as "forward" or Eulerian-to-Lagrangian coupling. At sufficiently high mass loadings, the particles begin to influence the fluid. This back effect represents Lagrangian-to-Eulerian or "backward" coupling.

---

 * Corresponding author. Address: Department of Mechanical and Aerospace Engineering, University of Florida, 231 MAE-A, P.O. Box 116300, Gainesville, FL 32611-6300, United States. Tel.: +1 352 392 0961; fax: +1 352 392 7303.
   E-mail addresses: yueling@ufl.edu (Y. Ling), haselbac@ufl.edu (A. Haselbacher), bala1s@ufl.edu (S. Balachandar).

To discuss the coupling in more detail, consider the momentum exchange between the phases. According to Newton's third law, the hydrodynamic force exerted on the individual particles is applied back to the carrier phase. In backward coupling, the forces from particles must be transferred to the grid points and applied as source/sink terms in the momentum equations of the carrier phase. A smooth distribution of the particle number-density, i.e., the number of particles per unit volume, on the grid is essential for an accurate accounting of the back effect of the dispersed phase on the carrier phase. Large grid-scale fluctuation in the particle number-density will introduce spurious small-scale oscillations in the carrier phase through backward coupling. These oscillations, in turn, will then be fed back to the particle motion and distribution through forward coupling. This feedback mechanism can lead to accumulation of errors.

Here, we focus on a class of physical problems where the particles are small and numerous. This will result in a large number of particles within each grid cell (in one dimension: the region between two adjacent grid points), allowing a conceptually smooth representation of the particle number-density and the backward coupling. Because the cost of Eulerian–Lagrangian simulations is proportional to the number of particles, it is common to limit the average number of particles per cell and define so-called "computational particles" that represent a large number (or cloud) of real particles. In such simulations, several sources of numerical errors can be identified:

(1) The Eulerian Discretization Error (EDE) that arises from the spatial and temporal discretization of the equations governing the carrier phase.
(2) The Interpolation Error (IE) that arises from the interpolation of the carrier-phase solution from the Eulerian grid to the particle locations.
(3) The Lagrangian Integration Error (LIE) that arises from the temporal discretization of the Lagrangian equations for the particles.
(4) The Back-Coupling Error (BCE) that arises partly from the discrete algorithm that apportions the momentum and energy coupling of the individual particles back to the neighboring grid points (or cells) and partly from the fact that only a limited number of computational particles are used to represent the true system where spatial distribution is random.

These errors are controlled by the spatial discretization, the temporal discretization, and the Lagrangian discretization (number of computational particles per cell). The errors from the spatial and temporal discretizations are easily controlled, at least in principle, by choosing appropriate methods and reducing the grid spacing Δx and time step Δt. For this reason, we ignore the EDE and LIE in the following. (All numerical results presented below have been verified to have negligible EDE and LIE.) The other two errors (IE and BCE) arise from the numerical approximation of the forward and backward coupling. Several interpolation schemes (second-, fourth-, and sixth-order Lagrange interpolation; spline interpolation; Hermite interpolation; etc.) have been used in the past. The IE arising from various interpolation schemes has been considered by [1] and [20] for turbulent flows. Although higher-order schemes have been shown to result in significantly reduced IE, lower-order methods such as trilinear interpolation are often used, especially in the context of finite-volume and finite-difference approaches (see, e.g., [16,15,21]). Similarly, several techniques have been advanced to back-couple the Lagrangian particles to the carrier phase, such as the particle-in-cell approach (e.g., [5,4,8]) and the projection method (e.g., [17,19,2]). The accuracy of backward-coupling algorithms has recently been examined by [7].

Eulerian–Lagrangian simulations of multiphase flows often exhibit small-scale fluctuations in the number-density. Here, the term "small scales" means scales on the order of the grid spacing. Traditionally, such fluctuations have been ascribed to two errors. If particles are randomly distributed with uniform probability over a given domain, the inherent stochastic fluctuation arising from the random distribution will contribute to grid-cell to grid-cell variation in the particle number-density. This *stochastic* error scales as the inverse square root of the mean number of particles per grid cell. A further error is due to the finite number of computational particles, which is typically far smaller than the actual number of particles. This *deterministic* error decreases as the inverse of the mean number of particles per grid cell (see [13,22,7]). Thus, while the nature of these two errors is fundamentally different, both can be controlled by increasing the number of computational particles.

However, there are cases (see [10]) where small-scale number-density fluctuations cannot be reduced by increasing the number of computational particles or by maintaining the number of computational particles in each cell constant (see [13,18,9,12]). Furthermore, these small-scale fluctuations cannot be explained on the basis of stochastic errors arising from a random particle distribution. It is this additional of error in particle number-density that is the focus of this article.

A simple explanation for the added source of number-density fluctuation that cannot be reduced by increasing the number of particles is as follows. Consider the carrier-phase velocity to consist of a simple propagating disturbance of fixed shape and size. Let the exact fluid velocity be known at the grid points at all time instances (i.e., EDE is taken to be zero at the discrete grid points). Even then, if a lower order interpolation scheme is used to obtain fluid velocity between grid points for computing particle motion, the resulting interpolated fluid disturbance will change shape as it propagates through the grid. This interpolation error in particle motion contributes to spurious variations of the particle position at the subgrid scale. These variations may accumulate over time and become significant. Thus, particle number-density error can arise from interpolation error (IE) even in the absence of any error in the fluid solution (EDE). However, in any typical numerical implementation, the fluid velocity will include Eulerian discretization error and if the spatial discretization of the flow solver and the interpolation scheme are of the same order then EDE and IE will be comparable. Both EDE and IE will lead to errors in particle number-density.

As will be shown below the nature of interpolation error's impact on particle motion will be such that IE will result in spurious small-scale fluctuation in particle number-density. This error will be subgrid in origin and appear as fluctuating clustering of particles within the grid cells. There are situations where particles tend to preferentially accumulate and create regions of enhanced concentration and regions devoid of particles, either due to their inertial effect or due to non-zero divergence of the underlying fluid velocity. Such effective divergence in particle motion spreads the subgrid error due to IE and give rise to grid-cell to grid-cell particle number-density fluctuation.

The goals of this article are (1) to determine the precise source of the error, (2) to demonstrate how the error can be reduced, and (3) to characterize the error magnitudes so that guidelines can be established that allow practitioners to keep the error below specified thresholds. The overall approach adopted to reach these goals is to systematically eliminate other sources of error, consider four simple test problems in one dimension. The first two are model problems where the propagating fluid disturbance consists of (1) a single sinusoidal wave and (2) a hyperbolic-tangent disturbance. These two models problems provide the ideal test bed to illustrate the interpolation-induced error in particle number-density. While the former has no net fluid-velocity divergence across the disturbance, the later does. This allows examination of how subgrid error translates to grid-cell to grid-cell error. The later two test cases consider one-dimensional compressible flows of practical interest, namely (3) an expansion fan and (4) a shock wave. The results obtained from the model problems will be used to interpret the results for these later test cases.

The remainder of this article is structured as follows. The general mathematical model of multiphase flow in Eulerian–Lagrangian framework is described in Section 2. A simplified model is introduced in Section 3. The numerical approach is outlined in Section 4. Results are presented in Section 5. Conclusions are offered in Section 6.

2. Mathematical formulation

The equations governing the carrier phase are conveniently expressed in the Eulerian frame of reference. We consider only one-dimensional problems in this article because the fundamental nature of the error investigated here is not dependent on the number of spatial dimensions. The mass, momentum, and energy equations of the carrier phase can then be written as

$$\frac{\partial(\rho^{g*})}{\partial t^*} + \frac{\partial(\rho^{g*}u^{g*})}{\partial x^*} = 0, \tag{1}$$

$$\frac{\partial(\rho^{g*}u^{g*})}{\partial t^*} + \frac{\partial[\rho^{g*}(u^{g*})^2]}{\partial x^*} = -\frac{\partial p^{g*}}{\partial x^*} - f^{p*}, \tag{2}$$

$$\frac{\partial(\rho^{g*}E^{g*})}{\partial t^*} + \frac{\partial(\rho^{g*}H^{g*}u^{g*})}{\partial x^*} = -u^{p*}f^{p*} - q^{p*}, \tag{3}$$

where $\rho, u, p, E,$ and H represent the density, velocity, pressure, total energy, and total enthalpy. The superscripts g and p denote properties associated with the gas phase and particle phase, respectively. The superscript $*$ indicates dimensional quantities. The total enthalpy of the gas H^{g*} is given by $H^{g*} = E^{g*} + p^{g*}/\rho^{g*}$. The ideal-gas law is assumed to apply, i.e.,

$$p^{g*} = (\gamma - 1)\rho^{g*}\left[E^{g*} - \frac{1}{2}(u^{g*})^2\right], \tag{4}$$

where γ is the ratio of specific heats of the gas. We use $\gamma = 1.4$ throughout.

The Lagrangian evolution equations for the particle position x^{p*}, velocity u^{p*}, and temperature T^{p*} are

$$\frac{dx^{p*}}{dt^*} = u^{p*}, \tag{5}$$

$$\frac{du^{p*}}{dt^*} = \frac{u^{g*}(x^{p*}, t^*) - u^{p*}}{\tau^{p*}}, \tag{6}$$

$$\frac{dT^{p*}}{dt^*} = \frac{T^{g*}(x^{p*}, t^*) - T^{p*}}{\tau_\theta^{p*}}, \tag{7}$$

where $u^{g*}(x^{p*}, t^*)$ and $T^g(x^{p*}, t^*)$ are the gas velocity and temperature at the particle location, respectively, and the particle mechanical and thermal time scales τ^{p*} and τ_θ^{p*} are given by

$$\tau^{p*} = \frac{\rho^{p*}(d^{p*})^2}{18\mu^{g*}}, \quad \tau_\theta^{p*} = \frac{C^{p*}\rho^{p*}(d^{p*})^2}{12\kappa^{g*}}, \tag{8}$$

where ρ^{p*} is the particle density, d^{p*} is the particle diameter, and C^{p*} is the particle specific heat, all of which are assumed to be constants. Because finite Reynolds number effects are not important for the purpose of this study, no such corrections are incorporated. The variation of the dynamic viscosity μ^{g*} with temperature is given by Sutherland's law. The conductivity κ^{g*} and viscosity of the gas are related by the Prandtl number $\Pr = \mu^{g*}C_p^{g*}/\kappa^{g*}$, where C_p^{g*} is the specific heat at constant pressure of the gas. In the limit $\tau^{p*} \to 0$, the particle behaves as a tracer and follows the local gas, i.e., $u^{p*} \to u^{g*}(x^{p*}, t^*)$. When $\tau^{p*} \neq 0$, particle inertia becomes important and the particle velocity differs from that of local gas phase velocity.

When the particle mass loading is not negligible, the particles influence the momentum and energy of the gas through f^{p*} and q^{p*} in Eqs. (2) and (3) (backward coupling). For the ith particle, we have

$$f_i^{p*} = \frac{\pi}{6} \frac{\rho^{p*}(d^{p*})^3}{V_{cell}^*} \frac{u^{g*}(x_i^{p*}, t^*) - u_i^{p*}}{\tau^{p*}}, \quad q_i^{p*} = \frac{\pi}{6} \frac{C^{p*}\rho^{p*}(d^{p*})^3}{V_{cell}^*} \frac{T^{g*}(x_i^{p*}, t^*) - T_i^{p*}}{\tau_\theta^{p*}}, \tag{9}$$

where V_{cell} is equal to the grid spacing for the one-dimensional computations considered here. The terms f^{p*} and q^{p*} in Eqs. (2) and (3) are calculated by summing f_i^{p*} and q_i^{p*} of all the particles in the vicinity of the grid point.

3. A simple model scenario

Though results based on the mathematical model described in Section 2 will be shown in Section 5, we consider an even simpler model first to isolate the precise cause for the small-scale number-density fluctuations. In this simpler model, we assume that the fluid velocity is a known function and that heat-transfer effects are negligible. Then only the solution of the particle position and momentum equations is required.

For reasons that will become clear below, a gas phase velocity disturbance that is spatially compact is particularly useful in the present study. Then the gas phase velocity can be written in dimensional form as

$$u^{g*}(x^*, t^*) = \begin{cases} 0 & \text{if } x^* + u_s^* t^* \leqslant -N^*/2 \\ \psi(x^* + u_s^* t^*) & \text{if } -N^*/2 < x^* + u_s^* t^* \leqslant N^*/2 \\ u_2^* & \text{if } x^* + u_s^* t^* > N^*/2, \end{cases} \tag{10}$$

where N^* is the region of support. The shape of the disturbance is dictated by the choice of the function ψ and is independent of time. As defined above, the disturbance travels leftward at a constant velocity of $u_s^* > 0$. The function ψ is defined to guarantee at least C^0-continuity at $x^* + u_s^* t^* = \pm N^*/2$. We assume that the particles are initially stationary, uniformly distributed within a given sub-domain, and to the left of the disturbance. The model problem is shown schematically in Fig. 1. Our primary interest is to determine how the particles are redistributed as the disturbance propagates through the particles.

It is instructive to first consider the theoretical behavior of the particles in reaction to the disturbance. The particles remain stationary until the arrival of the disturbance. We place a restriction on the gas phase velocity that $\psi + u_s^* > 0$ for all x^*. This ensures that there are no fixed points in Eqs. (5) and (6) where particles can accumulate. Thus, as the disturbance moves to the left, the particles are guaranteed to emerge from the disturbance on the right. For a tracer particle, i.e., for $\tau^p = 0$, the velocity instantaneously becomes equal to u_2^* as soon as the disturbance moves past it. For an inertial particle, i.e., for $\tau^p > 0$, the approach to the velocity is asymptotic. In the region of the disturbance where the particle velocity is varying, the spacing between particles can be non-uniform. But to the far right of the disturbance, where the particle velocity has reached the asymptotic value of u_2^*, the particles are again uniformly distributed. From conservation of particles, it can be shown readily that the ratio of the uniform spacing between two adjacent particles after the passage of the disturbance to that before the disturbance is $1 + u_2^*/u_s^*$.

In what follows, it will be shown that the above theoretical results are not recovered when the problem is solved numerically. Although all the particles numerically reach the correct asymptotic velocity of u_2^*, they will not be uniformly distributed. It is this non-uniform distribution of particles that can give rise to the grid scale fluctuations described in the introduction. The root cause of the error lies in the precise way in which the fluid velocity is interpolated to the particle location. In the numerical solution, the fluid velocity that is collocated at the grid points is interpolated to obtain a numerical approximation to ψ. As the disturbance moves through the fixed Eulerian grid, the interpolated fluid velocity varies over time (i.e., the numerical approximation to ψ varies). This variation is time-periodic, since the fluid velocity at the grid points and its interpolation are identical after the disturbance has moved over an entire grid cell.
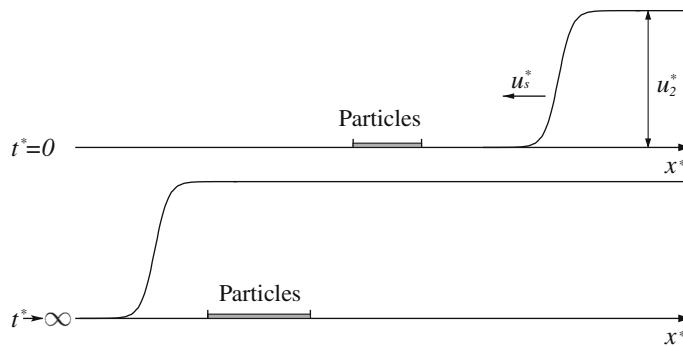

Fig. 1. Schematic of model problem in which a wave moves through a packet of particles. In model problem 1 (see Section 5.1), a sinusoidal wave is considered. In model problem 2 (see Section 5.2), a hyperbolic-tangent wave is used.

In essence, although the exact disturbance is collocated at the grid points as it propagates to the left, its numerical approximation obtained from interpolation changes as the disturbance moves within a grid cell, and this variation cyclically repeats over adjacent grid cells. Consequently, particles that are initially located at different positions within a grid cell "see" slightly different histories of the carrier-phase velocity as the disturbance propagates through the grid cell. This results in a non-uniform particle distribution as they emerge out of the disturbance. Again, the non-uniformity is within a *packet of particles* that was between grid points to the left of the disturbance before its arrival. By contrast, in the exact solution, there is no grid dependence and each particle sees the same history of gas phase velocity and thus a uniform spacing is preserved even after particles emerge from the disturbance.

A key parameter that controls the level of non-uniformity in the numerical solution is the grid size Δx^*, or more precisely the number of grid points used to resolve the disturbance ($N = N^*/\Delta x^*$). Here we use the grid size Δx^* and the velocity of propagation of the disturbance u_s^* as the length and velocity scales. Then the gas phase velocity and the equations of motion for the particle can be written in dimensionless form as

$$u^g = u^g(x, t),$$ (11)

$$\frac{dx^p}{dt} = u^p,$$ (12)

$$\frac{du^p}{dt} = \frac{u^g(x^p, t) - u^p}{\tau^p},$$ (13)

where the variables without superscripts $*$ are dimensionless.

4. Approach

4.1. Numerical methods for governing equations

For the model problem, the gas solution is assumed to be known and is not influenced by the particles, i.e., we only consider one-way coupling. For the real multiphase-flow problems, both the gas and the particle phases need to be solved. In this work, Eqs. (1)–(3) are solved by a fifth-order accurate hybrid compact-WENO scheme with RK4 time integration described by [3]. Eqs. (5)–(7) are integrated in time with RK4 also. The grid spacing and time step are chosen small enough to ensure that the associated errors are negligible. The implementation of two-way coupling is described by [10,11].

4.2. Interpolation methods

In the numerical integration of Eqs. (6) and (7) or Eq. (13), fluid quantities at the particle position, e.g., $u^{g*}(x^{p*}, t^*)$ or $u^g(x^p, t)$, are needed. They must be obtained through interpolation from grid-point values of the fluid velocity. In the present study, we employ four interpolation methods:

(1) *Piecewise-constant interpolation*: The interpolated fluid velocity is approximated as a constant between grid points and is therefore discontinuous at the grid points. The fluid velocity at the particle location is obtained by averaging the values at the two grid points straddling the cell in which the particle is located. This interpolation scheme is not of practical interest due to its low order of accuracy.
(2) *Piecewise-linear interpolation*: This interpolation method can be viewed as first-order spline interpolation. The fluid-velocity distribution inside a cell is approximated as linear. The interpolated fluid velocity is only C^0-continuous across the grid points. In two and three dimensions, this scheme leads to the widely used bilinear and trilinear interpolation schemes.
(3) *Natural cubic-spline interpolation:* In cubic-spline interpolation, the fluid velocity is constructed such that the interpolated fluid velocity is smooth and continuous in the first and second derivatives at the grid points. Natural cubic splines, which assume that the second derivatives of the interpolant at the domain boundaries are zero, are the most commonly used cubic spline.
(4) *Hermite interpolation:* In this method, the fluid velocity inside a cell is interpolated by Hermite polynomials. Therefore, not only the function values but also the first derivative are needed at the grid points. The interpolated fluid velocity is C^1-continuous. In the model problems, the first derivative at the grid points is available analytically. In a real computation, the first derivative of the fluid velocity at the grid points must be computed numerically. In multiple dimensions, the complete implementation of Hermite interpolation can be tedious, and instead, a simpler shape-function method can be used see [1].

4.3. Error definitions

To evaluate the influence of the interpolation error and the resulting non-uniformity in the particle distribution, we only need to study a single *packet of particles*, defined as a group of particles located within a grid cell prior to the arrival of the

disturbance. As discussed above, and to be illustrated in more detail below, the behavior of each packet of particles is identical.

We define the right and left bounds of the packet as $x_R^p(t)$ and $x_L^p(t)$, respectively. The distribution of particles in the packet at any given time is a function of the initial distribution. Thus the distribution of particles within the packet can be defined in terms of their relative-position as follows:

$$\eta(\eta_0, t) = \frac{x^p(t) - x_L^p(t)}{x_R^p(t) - x_L^p(t)}, \tag{14}$$

such that $0 \leqslant \eta \leqslant 1$ at all times. Similarly, the initial distribution of particles within the packet is given by

$$\eta_0 = \frac{x^p(0) - x_L^p(0)}{x_R^p(0) - x_L^p(0)}. \tag{15}$$

Therefore, $\eta = \eta(\eta_0, t)$ gives the particle distribution inside the packet and serves as a mapping from the initial to the current particle distribution.

The derivative $d\eta/d\eta_0$ measures the particle spacing, i.e., the distance between two neighboring particles within the packet. The inverse of the particle spacing, i.e., $d\eta_0/d\eta$, provides a measure of the local particle number-density. The particle number-density within a grid cell of unit width centered around η can then be obtained as

$$n^p(\eta) = \frac{1}{\theta} \int_{\eta-\theta/2}^{\eta+\theta/2} \frac{d\eta_0}{d\eta}\bigg|_\xi d\xi, \tag{16}$$

where $\theta = 1/(x_R^p(t) - x_L^p(t))$ is the unit grid spacing normalized by the current packet size $x_R^p(t) - x_L^p(t)$.

We define several errors to measure the small-scale fluctuations arising from the interpolation. In all definitions, we compare the numerical results (subscript "*num*") with the corresponding exact solution (subscript "*ex*"). For the exact solution, the asymptotic particle distribution remains uniform as discussed above, and we have the results $\eta_{ex}(\eta_0, t) = \eta_0$ and $(d\eta/d\eta_0)_{ex} = 1$ as $t \to \infty$. However, the width of the packet of particles changes and the ratio of final to initial number-density is given by $1/(1 + u_2)$. The error definitions are:

- *Mean error:* Measures the error in the mean location of the packet,

$$E_{mean} = \frac{1}{L}\left(\frac{x_{L,ex}^p + x_{R,ex}^p}{2} - \frac{x_{L,num}^p + x_{R,num}^p}{2}\right). \tag{17}$$

- *Spread error:* Measures the error in the width of the packet,

$$E_{spr} = \frac{\left(x_{R,ex}^p - x_{L,ex}^p\right) - \left(x_{R,num}^p - x_{L,num}^p\right)}{\left(x_{R,ex}^p - x_{L,ex}^p\right)}. \tag{18}$$

- *Relative-position error:* Evaluates the error of the relative particle position within the packet compared to the exact solution,

$$E_{pos}(\eta) = |\eta - \eta_0|. \tag{19}$$

- *Spacing error:* Evaluates the error in adjacent particle spacing,

$$E_{spac}(\eta) = \left|\frac{d\eta}{d\eta_0} - 1\right|. \tag{20}$$

- *Number-density error:* Evaluates the error in particle number density within each grid cell arising from the numerical solution,

$$E_{nd}(\eta) = |n^p(\eta) - 1|. \tag{21}$$

Note that the relative-position, spacing, and number-density errors are defined as a function of the current relative particle position. To measure the error for the entire packet of particles, the L_2- and L_∞-norms are used,

$$L_2(E) = \int_0^1 (E(\eta))^2 d\eta, \tag{22}$$

$$L_\infty(E) = \max_\eta |E(\eta)|, \tag{23}$$

where E stands for E_{pos}, E_{spac}, or E_{nd}. In the above definitions, the particle distribution in a packet is assumed to be continuous. Therefore, the error definitions are independent of the number of particles within the packet, and hence the Lagrangian discretization does not play a role. When calculating the above error norms numerically, finite numbers of particles are used.

The numbers of computational particles used in all the calculations reported below have been chosen large enough to resolve the continuous error profile inside the packet. As a result, any errors due to finite numbers of particles are negligibly small compared to the interpolation error.

5. Results

In this section, results for four test problems are presented. The first two problems are model problems of the kind described in Section 3 with sinusoidal and hyperbolic-tangent profiles, respectively. The primary difference between the two profiles is that the latter has non-zero net fluid-velocity divergence and, therefore, represents a simple model for compression and expansion waves. The second two problems are based on the full Euler equations for the gas phase listed in Section 2 and consider proper expansion and shock waves.

5.1. Test problem 1: Sinusoidal profile

The fluid velocity is taken to be a single sinusoidal wave that moves to the left at unit speed u_s^* into a particle packet, as shown schematically in Fig. 1. The non-dimensional fluid velocity is

$$u^g(x,t) = \begin{cases} A\sin\left[\frac{2\pi(x+t)}{N}\right] & \text{if } -t - N/2 \leqslant x \leqslant -t + N/2, \\ 0 & \text{else}, \end{cases} \tag{24}$$

where N denotes the number of grid points across the unit wavelength of the sinusoidal wave and $A = A^*/u_s$ is the dimensionless amplitude. Note that A must be smaller than unity to avoid particle settling at fixed points. N provides a measure of how well the carrier-phase velocity is resolved by the computational grid. The fluid velocity defined by Eq. (24) is only C^0-continuous because of slope discontinuities at the head and tail of the wave. To reduce interpolation errors near these discontinuities, it is assumed that the head and tail positions are known to subgrid resolution. Therefore, the fluid velocity is only interpolated over the domain $-t - N/2 \leqslant x \leqslant -t + N/2$ and taken to be zero elsewhere. An important characteristic of this model problem is that the particle velocity returns to zero after the passage of the disturbance, i.e., $u_2 = u_2^*/u_s^* = 0$. Therefore, the net divergence of fluid velocity is zero, and the non-dimensional packet width returns to its starting value of unity. The results presented below can be interpreted as a von-Neumann-type error analysis of particle redistribution within the packet and used to evaluate the accuracy of interpolation schemes.

In this model problem, the key parameters are N, τ^p, and A. We only consider tracer particles, i.e., $\tau^p = 0$. We first demonstrate the effect of interpolation error with a case of very poor spatial resolution, namely $N = 4$ and $A = 0.5$.

5.1.1. Particle redistribution

The fundamental source of non-uniform particle redistribution within a packet is due to the manner in which the interpolation scheme approximates the sinusoidal fluid-velocity disturbance as the latter propagates through the fixed Eulerian grid. Fig. 2 shows the exact velocity profile and its approximation by the four interpolation schemes. In non-dimensional terms, the wave propagates to the left by one grid spacing in unit time. For ease of interpretation, each figure is centered about the wave and the grid locations are marked by black filled circles. Several observations can be made. First, as expected, the interpolation error decreases as the order of interpolation increases, with the largest error observed for piecewise constant interpolation. The error is particularly large in Fig. 2 since only four points are used to resolve the wave. More significant than the error itself is how the error changes in time. As the sinusoidal disturbance moves through the grid, the collocated values at the grid points vary in time. The numerical representation of the disturbance obtained from the interpolation changes correspondingly. This change can be observed readily in the different shapes of the lower-order interpolants. Although not as readily observable, the approximations changes with time even for the higher-order spline and Hermite interpolations. This variation in the approximation to the fluid velocity repeats after the wave has moved by one grid spacing.

The adverse impact of the periodic variation in the interpolated fluid velocity on particle motion and redistribution can now be addressed. When the leading edge of the wave reaches a given particle, it starts to move due to the non-zero relative velocity. When a given particle exits the wave, it decelerates back to zero velocity. The tracer particles considered here stop moving once they reach the tail of the sinusoidal wave. Thus, each particle "sees" a history of fluid velocity that dictates its motion and final resting position. Due to variation in the interpolated sinusoidal wave, as illustrated in Fig. 2, the history of fluid velocity "seen" by a given particle will depend on its initial position relative to the grid. As a result, an initially uniform distribution of particles between two grid points will not remain uniformly distributed.

In interpreting the results, it is important to distinguish between two components of the interpolation error. The first is the mean interpolation error that affects all particles irrespective of their initial location within the packet. The effect of this error is that the final numerically predicted position of a particle within the packet is different from its exact position. Because this error is the same for all particles within a packet, it does not affect the uniformity of particle distribution. The second error, which is that of primary concern here, is that component of the interpolation error that changes as the wave passes through the fixed grid. Since the mean error has been taken into consideration, this error can be thought of as the fluctuating interpolation error. The fluctuating interpolation error is the sole cause of the non-uniform particle distribution.
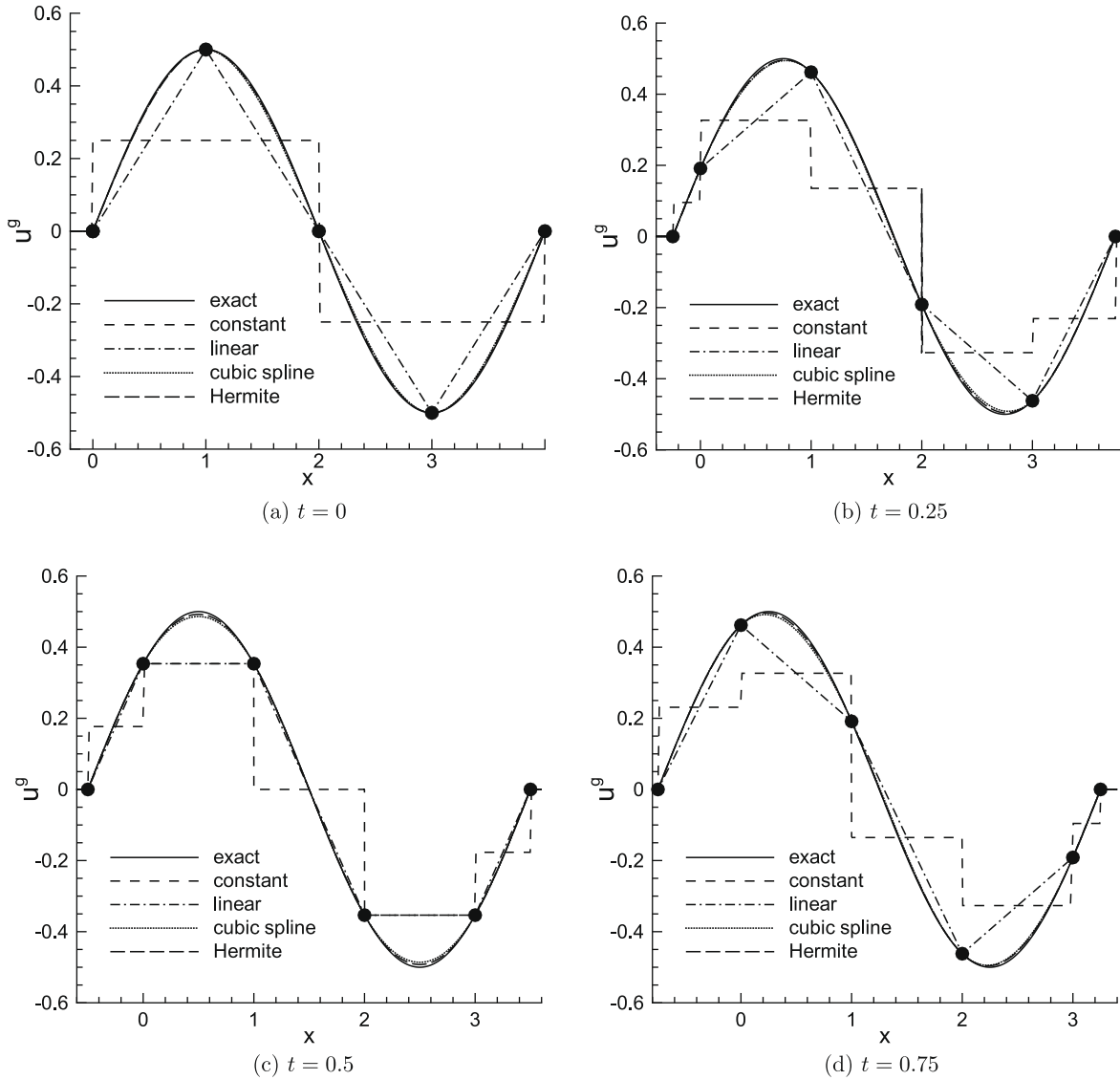
Fig. 2. Exact and interpolated fluid-velocity profiles as a function of time for $N = 4$ and $A = 0.5$. The filled circles denote locations with collocated values.

Fig. 3(a) shows the final particle position and its error compared to the exact solution as a function of the initial particle position. From this figure, both the mean and the relative-position error of the particles can be discerned. According to the exact solution, every particle shifts to the left by 0.6188 because of the passage of the sinusoidal wave. By comparison, the average left-shifts of the particles in the numerical solutions are 0.1910 (69.14%), 0.3690 (40.36%), 0.5983 (3.31%) and 0.6070 (1.90%), respectively, for the piecewise constant, piecewise linear, spline, and Hermite interpolations (the mean-position percentage errors are given in parentheses). The variation in the position error as a function of the initial particle location presented in Fig. 3(b) is responsible for the non-uniform distribution of particles. Note that the error repeats for every packet of particles initially located between grid points. Therefore, we will focus on the behavior of a single packet for the rest of the article. The results presented below can be extended to distributions stretching over multiple grid spacings by applying periodicity.

Fig. 4(a) gives the relative-position η of a particle inside the packet as a function of its initial relative-position η_0 and the various interpolation methods. The exact solution is simply $\eta = \eta_0$. The error in the relative particle position translates into an error in spacing between adjacent particles $d\eta/d\eta_0$ and hence into an error in local particle number-density $d\eta_0/d\eta$. The local particle number-density is presented in Fig. 4(b) for the various interpolation schemes. As can be expected, the errors associated with piecewise-constant interpolation are large. For instance, in Fig. 4(a), it can be seen that the relative-position remains nearly constant at $\eta \approx 0.92$ for $0.5 \leqslant \eta_0 \leqslant 0.95$. In other words, particles that were originally distributed over nearly half the packet are concentrated in a narrow region around $\eta \approx 0.92$ after the passage of the wave. The corresponding sharp
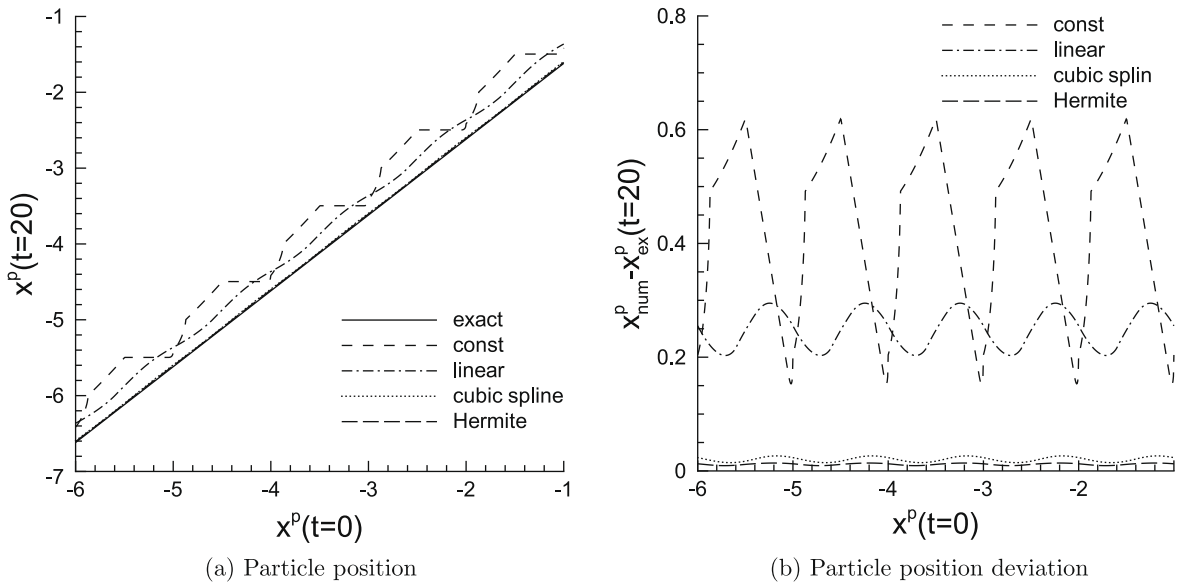
Fig. 3. Profiles of particle position and deviation from the exact solution at $t = 20$ as a function of initial position for $N = 4$, $\tau^p = 0$, and $A = 0.5$.
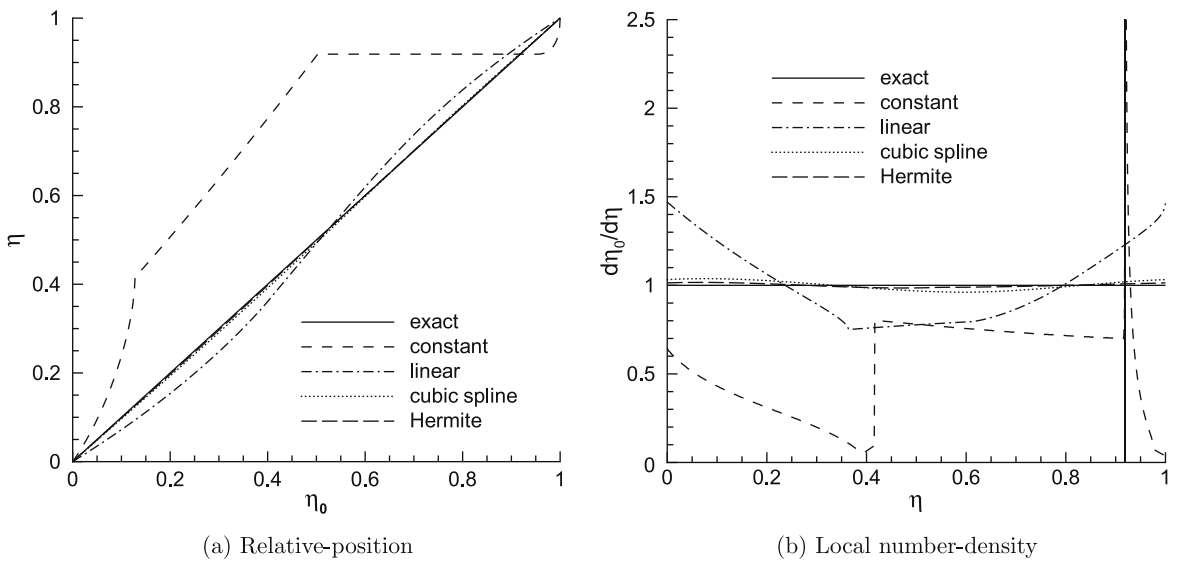

Fig. 4. Profiles of particle relative-position and local number-density inside the particle packet with initial size unity after the passage of the sinusoidal wave for $N = 4$, $\tau^p = 0$, and $A = 0.5$.

increase in local number-density can be observed in Fig. 4(b). The relative-position error for the piecewise linear interpolation is not nearly as large. Nevertheless, it can be seen in Fig. 4(b) that the local number-density varies from about 0.7 to 1.5. The corresponding errors for the spline and Hermite interpolation are small. Fig. 5 shows the relative-position and spacing errors of particles inside the packet for the different interpolation schemes. Note that the scalings of the ordinates are different. It is observed that the error of the piecewise-linear scheme is about an order of magnitude lower than the piecewise-constant interpolation and the corresponding errors of the natural cubic spline and Hermite interpolation methods are three orders of magnitude lower.

5.1.2. Global error norms

The global errors integrated across the entire packet as defined by Eqs. (22) and (23) are presented in Fig. 6. We observe that the rate of decay of the L_2-norm of the relative-position and spacing errors is consistent in general with the order of accuracy of the interpolation. The only exception is the result for piecewise-constant interpolation, for which the rate of decay seems smaller than $O(1)$. The lower error and the faster decay makes higher-order interpolation schemes attractive. For a
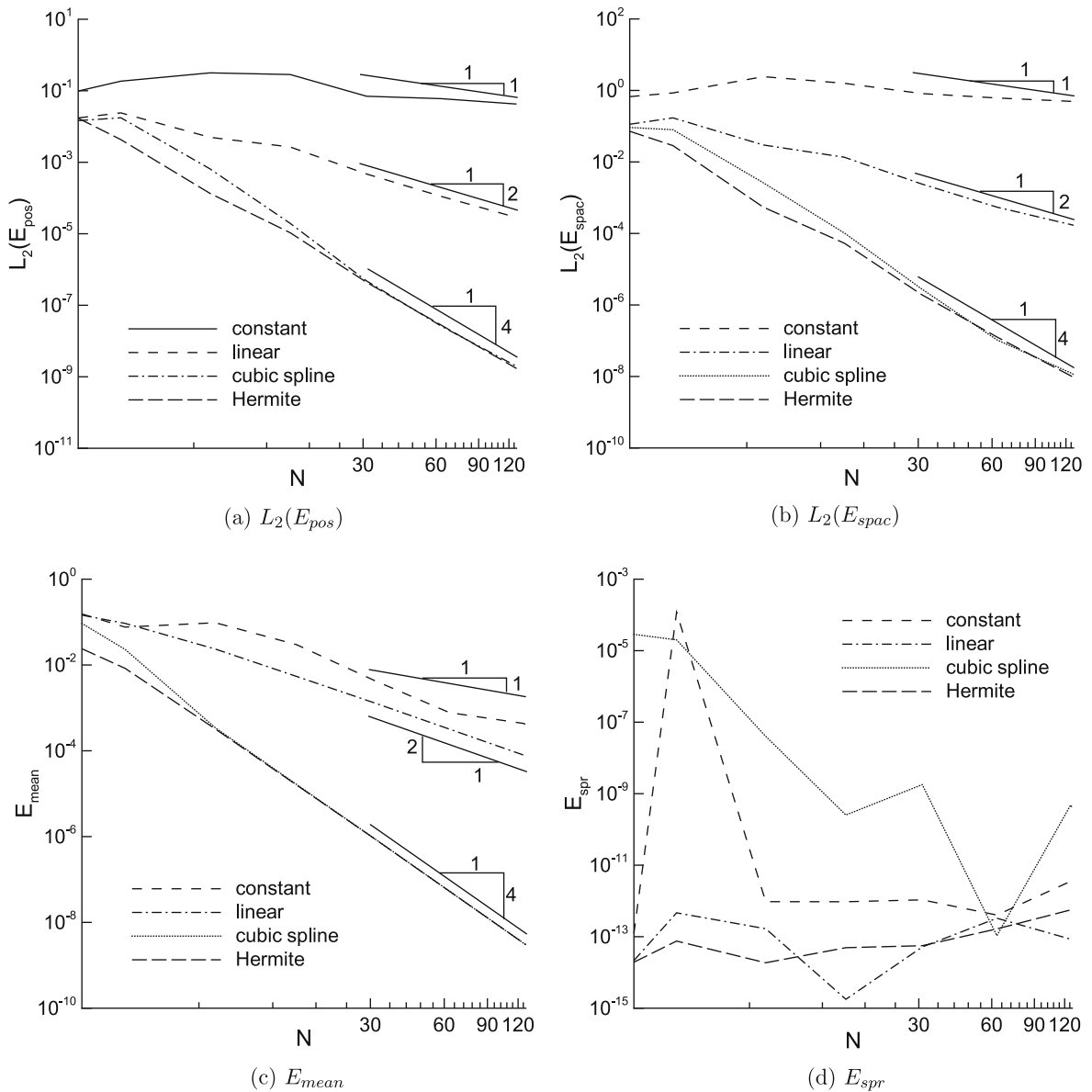
Fig. 6. Evolutions of the relative-position, spacing, mean, and spread errors $(E_{pos}, E_{spac}, E_{mean}, E_{sp})$ as functions of N for $\tau^p = 0$ and $A = 0.5$.

value. The objective is to show that because of this non-zero particle velocity divergence the sub-packet fluctuation of relative-position error will result in substantial grid-to-grid fluctuation in the number-density. Non-zero divergence of the fluid velocity is common in compressible flows. For example, expansion and compression waves have positive and negative divergence, respectively. Therefore, when an expansion fan or a shock wave pass through a region of uniformly distributed particles, significant concentration fluctuation can be expected based on the results of the first model problem.

Here, we take the fluid-velocity profile to be a hyperbolic-tangent function. With the same length and velocity scales as in the previous problem, the dimensionless fluid velocity can be written as

$$u^g(x, t) = \frac{u_2}{2}\left[1 + \tanh\frac{2(x+t)}{N}\right], \tag{25}$$

where u_2 denotes the velocity jump and N represents the number of grid points across the thickness of the profile. Note that the fluid velocity has a smooth but sharp transition around $x + t = 0$ and that $u^g(x \to -\infty) = 0$ and $u^g(x \to +\infty) = u_2$, i.e., the fluid velocity on both sides is constant far away from the jump. When $u_2 > 0$, Eq. (25) can be used to model an expansion fan with constant (or "frozen") thickness. Conversely, when $u_2 < 0$, Eq. (25) models a shock wave. Of course, it is physically inconsistent to have an expansion fan of constant thickness, since the width of a real expansion fan increases in time. Nev-

ertheless, this model problem is useful in providing insight into how an expansion fan can contribute to concentration fluctuations. The constant thickness of the expansion fan simplifies the interpretation of the results. A shock wave of constant thickness propagating through a distribution of particles is realizable, however, because of the opposing mechanisms of smoothing through diffusion and steepening through non-linearity.

5.2.1. Particle redistribution

When the wave reaches a particle, the latter starts to move to the right or left depending on the sign of u_2. After sufficiently long time, the hyperbolic-tangent wave has passed completely and the particle reaches the terminal velocity of u_2. After the particle packet reaches the steady state, it can be shown that the size of particle packet changes to $1 + u_2$. Therefore, the packet expands or contracts depending on whether u_2 is positive or negative. However, when the interpolated fluid velocity is used, the particles are redistributed in a non-uniform manner as for the sinusoidal-wave problem. The key parameters for this problem are N, τ^p, and u_2. Seven cases are presented for the values of τ^p and u_2 shown in Table 1.

Fig. 7 shows the relative-position η and local number-density $d\eta_0/d\eta$ variation inside a packet of particles for cases 2-1 and 2-2. Here $N = 4$, i.e., the thickness of the hyperbolic-tangent profile is resolved with only four grid points. Similar to the previous problem, for both expansion and compression, the interpolation error redistributes the particles and generates errors in the relative particle position and hence in the number-density. Fig. 8 presents the relative particle-position and spacing errors for cases 2-1 and 2-2. Again the piecewise-constant interpolation yields the largest error, the error of the piecewise-linear interpolation is an order of magnitude lower, and the errors of the natural cubic spline and Hermite interpolations are two orders of magnitude lower still.

In case 2-1, $1 + u_2 = 2$, therefore, the particles that were initially located in one grid cell will be distributed over two cells after the passage of the wave. Then the sub-packet variation of the local number-density generates grid-to-grid variation in particle number-density with a wavelength of two grid cells. A schematic of this situation is shown in Fig. 9(a) to demonstrate how the grid-to-grid number-density fluctuation is generated. In case 2-2, $1 + u_2 = 0.5$, hence the particles that were initially in one cell will be distributed over half a grid cell. So despite the sub-packet fluctuation due to the interpolation error, there will be no grid-to-grid number-density fluctuation, because the fluctuations will be contained at the subgrid level after the compression of the particles (see Fig. 9(b)). On the other hand, in case 2-3, where $1 + u_2 = 0.6$, the packet of particles that were initially distributed over one grid cell get compressed to 3/5 of a cell, resulting in a grid-to-grid fluctuation in particle number-density that is periodic over three grid cells as shown in Fig. 9(c). Therefore, we can state the following rule: If $1 + u_2$ is a rational number p/q, the sub-packet variation in particle distribution after the passage of the fluid-velocity disturbance will result in a grid-to-grid number-density variation that is periodic over p grid cells. If $1 + u_2$ is irrational, the grid-to-grid number-density variation will have no periodic structure.

5.2.2. Global error norm

Fig. 10 shows the relative-position, spacing, and mean errors for the different interpolation schemes for cases 2-1 and 2-3. In general, the errors decrease with increasing N and the rate of decay is consistent with the order of accuracy of the interpolation scheme. The only exception is the mean error, where N^{-2} behavior is observed for the piecewise-constant interpolation. However, recall that the mean error has no influence on the number-density fluctuation. Except for small N, the errors for cases 2-1 and 2-3 cases are nearly identical. Unlike for test problem 1, here we can compute the number-density error. Fig. 11 shows that the errors for Case 2-1 (the expansion wave, $u_2 = 1$) are consistently larger than those for Case 2-3 (the shock wave $u_2 = -0.4$).

It can be observed that the error of Hermite interpolation is smaller than that of the natural cubic spline interpolation when N is small. Note that the natural cubic spline interpolation behaves even worse than the piecewise-linear interpolation. When N is close to 1, the discretized hyperbolic-tangent profile appears as a discontinuity. As is well-known, higher-order interpolation schemes generate spurious oscillations in the interpolant near discontinuities. These spurious oscillations also vary in time and contribute to the redistribution of particles. Compared to the natural cubic spline, Hermite interpolation takes advantage of the exact first derivatives in constructing the interpolant, and hence performs much better for small N. Furthermore, Hermite interpolation better localizes the influence of the discontinuity, whereas the cubic spline tends to spread the interpolation error to a larger domain.
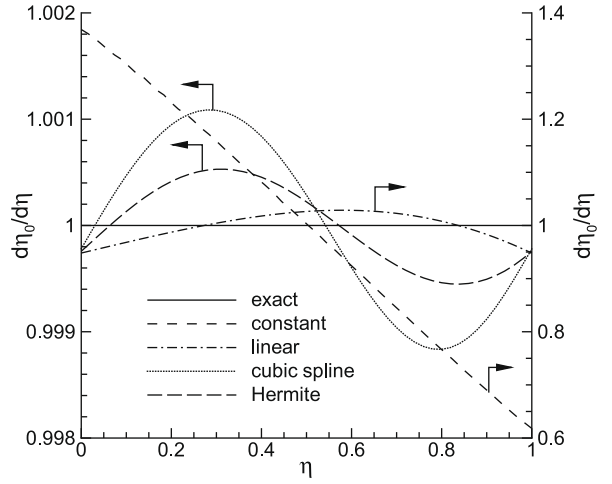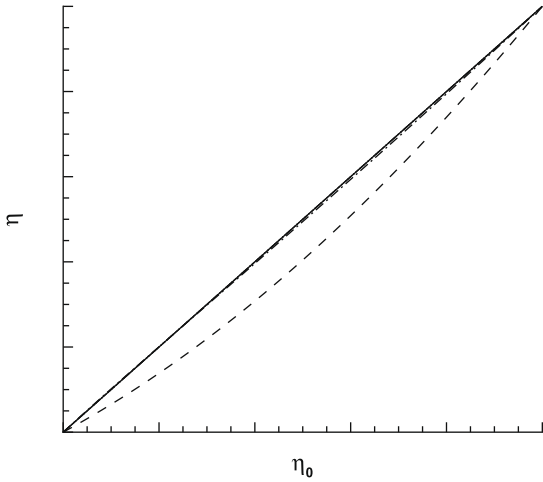
Table 1
Summary of cases for test problem 2.

Case	τ^p	u_2
2-1	0	1.0
2-2	0	−0.5
2-3	0	−0.4
2-4	0	0.1
2-5	0	10.0
2-6	1	1.0
2-7	10	1.0
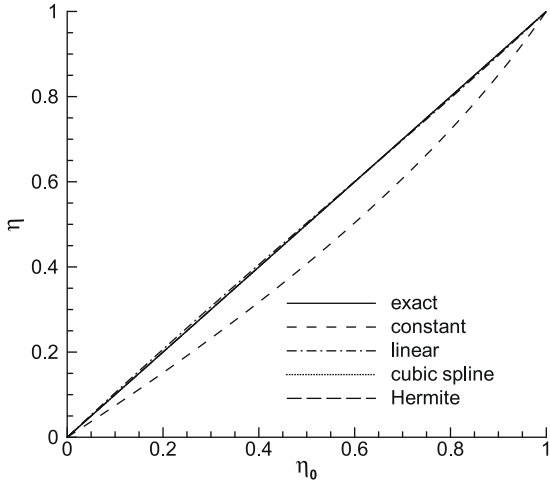
(a) Case 2-1: Relative-position

(b) Case 2-1: Local number-density

5.2.3. Effect of disturbance magnitude

The velocity jump or disturbance magnitude u_2 across the hyperbolic tangent is an important parameter. For given values of N, especially small ones, the larger u_2, the larger the velocity gradient, and hence interpolation is more challenging. Fig. 12 shows the variation of the error measures as a function of N for the disturbance magnitudes $u_2 = \{0.1, 1, 10\}$. All the errors presented in Fig. 12 decay with increasing N at the asymptotic rate dictated by the respective orders of the interpolation schemes. For the relative-position and spacing errors, the effect of u_2 is significant only at small values of N, i.e., when the hyperbolic- tangent profile is not well resolved. At large values of N, the errors become independent of u_2. The number-density error, however, seems to increase with increasing u_2. For small values of u_2, e.g., $u_2 = 0.1$, the errors are typically smaller for small values N and the approach to the asymptotic power-law behavior occurs only for $N \gtrsim 30$. The superior performance of higher-order interpolation is clear. For instance, if the grid-to-grid number-density fluctuation needs to be contained below 10^{-4}, less than 10 grid points are required to resolve the hyperbolic-tangent profile with the two higher-order schemes, while 70–100 grid points are required with piecewise-linear interpolation.

The natural cubic-spline interpolation does not work well for large u_2 and small N. It can be seen from Fig. 12(c), that for $u_2 = 10$ and small N, natural cubic-spline interpolation introduces an error comparable to or even larger than that for piecewise-linear interpolation. The oscillations in the interpolant adversely affect the particle redistribution, causing large fluctuations in the particle position.

Hermite interpolation seems to be the best interpolation scheme for the current problem among the methods tested. It behaves well even for the extreme case of small N and large u_2. However, it should be kept in mind that in the present
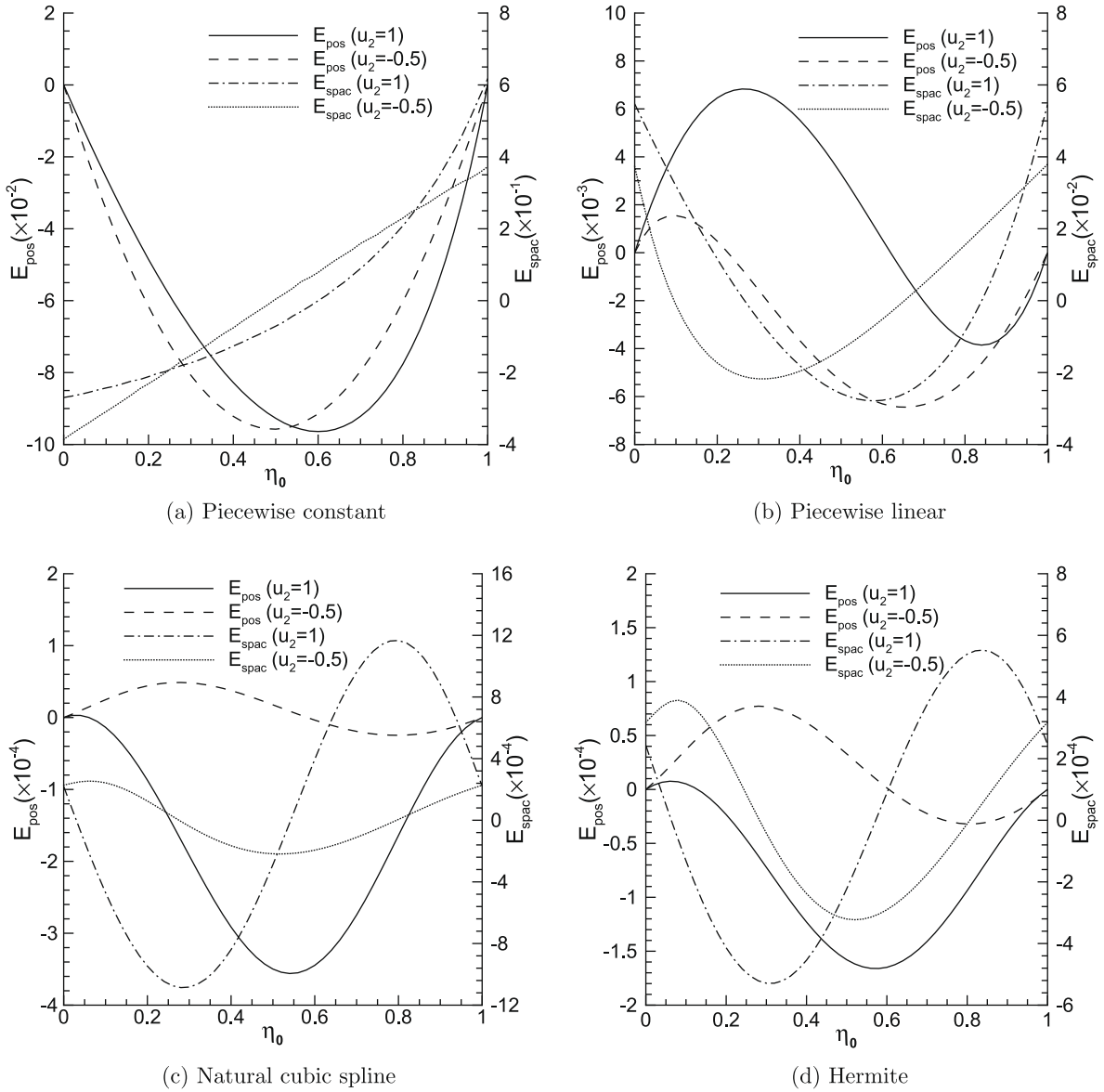
Fig. 8. Profiles of particle relative-position error and spacing error (E_{pos} and E_{spac}) inside the particle packet with initial size unity for cases 2-1 and 2-2 with $N = 4$.

implementation, the analytical first derivative is used by taking advantage of the known fluid-velocity profile. In a real computation, the first derivative is not known and must be calculated from the function values. Furthermore, the problem observed with the cubic-spline interpolation can also affect the Hermite interpolation. [6] developed a method of computing the first derivative that can guarantee monotonic interpolants. With this method, numerical oscillations in the interpolant upstream and downstream of the wave can be eliminated, guaranteeing that Hermite interpolation works well even for poor resolution.

5.2.4. Effect of particle inertia

We now consider inertial particles. The equation of motion for the particles only includes the Stokes-drag term and thus the dimensionless particle response time τ^p is the only parameter representing the particle-inertia effect. We choose cases 2-6 and 2-7 ($\tau^p = \{1, 10\}$), and compare them with case 2-5 ($\tau^p = 0$).

The results for the position, spacing, and number-density errors integrated across the packet are shown in Fig. 13 as a function of N and τ^p. For large N, the errors seem to be the lowest for the tracer particles and increase with increasing particle inertia. For very large N, the influence of τ^p is smaller than that of the interpolation scheme.

(a) case 2-1: $1 + u_2 = 2$
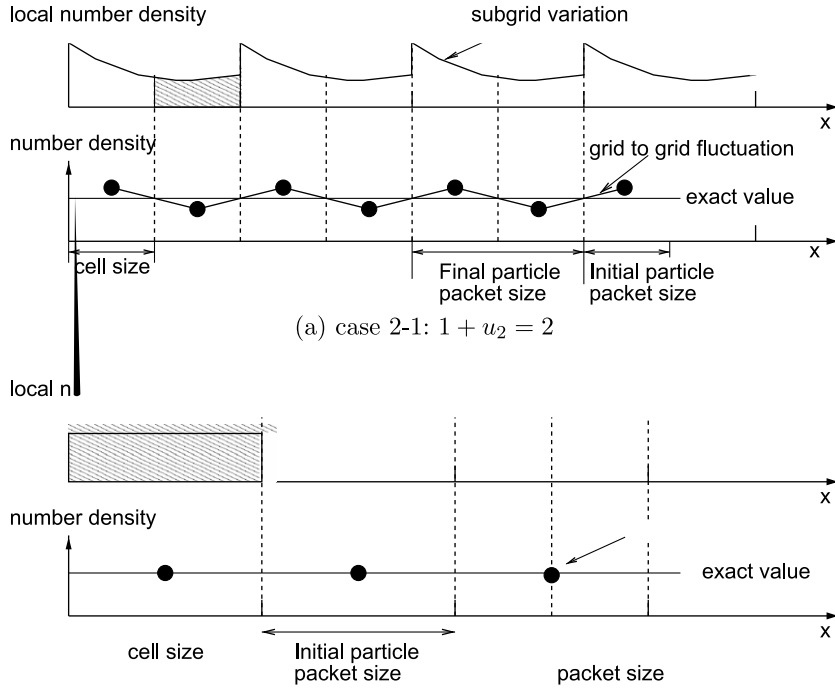
The error behavior reverses for small N and as a result the deviation of the inertial particles from the tracer particles is not monotonic. It can be observed clearly that the error for the inertial particles crosses that for tracer particles at a certain value of $N = \widehat{N}$. When $N < \widehat{N}$, the errors for inertial particles are smaller than for tracer particles. Conversely, when $N > \widehat{N}$, the opposite trend is observed. It is also interesting to note that $\widehat{N}$ decreases as the order of interpolation scheme goes down. In fact, for piecewise-constant interpolation the error for inertial particles is always larger than for tracer particles (i.e., $\widehat{N}$ does not exist). It seems for the higher-order interpolation schemes the inertial effect of particles helps reduce the particle number-density fluctuation when the grid resolution is poor.

5.3. Test problem 3: Expansion wave

We now extend the analysis from the model problems with imposed fluid-velocity profiles to problems in which the fluid velocity is obtained from numerical solutions of the Euler equations. First, we consider the propagation of a one-dimensional expansion fan into a particle-gas mixture. In contrast to the "frozen" expansion wave considered in Section 5.2, here the expansion-wave width increases with time. One particular focus of the following is to establish the degree to which the results obtained for the model problem apply to the real problem considered here.

The interaction of particles with expansion waves is of fundamental importance and has been investigated by [14] and [11]. We initialize the flow as a Riemann problem with the left and right states (denoted by subscripts 1 and 2, respectively) chosen such that an expansion fan with a pressure ratio of $p_1^{g*}/p_2^{g*} = 3.5$ and a temperature ratio of $T_1^{g*}/T_2^{g*} = 1.4$ results. The
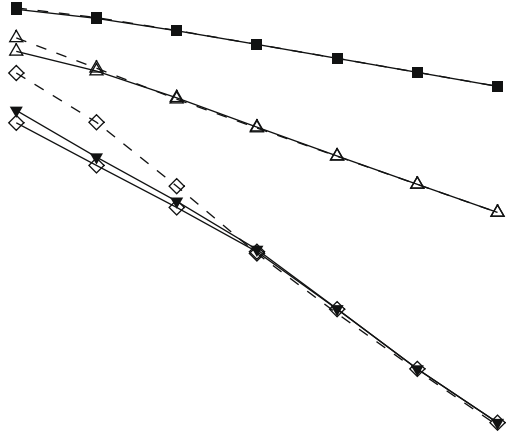
expansion region is initially of zero thickness, i.e., the pressure, density, and velocity exhibit discontinuities at $x = 0$. The head of the expansion fan propagates to the left at the speed of sound a_1^{g*}. The gas velocity increases across the expansion fan and reaches a constant value u_2^{g*} at the trailing edge, where

$$\frac{u_2^{g*}}{a_1^*} = \frac{2}{\gamma - 1}\left[1 - \left(\frac{p_2^{g*}}{p_1^{g*}}\right)^{\frac{\gamma-1}{2\gamma}}\right]. \tag{26}$$

With the above-stated conditions, we obtain $u_2^{g*}/a_1^* = 0.82$. The velocity of the tail of the expansion fan is given by $u_2^{g*} - a_2^*$, where the speed of sound a_2^* follows from the temperature ratio and hence $(u_2^{g*} - a_2^*)/a_1^* = -0.02$. Therefore, the flow out of the expansion fan is nearly sonic. The width of the expansion fan increases as $(u_2^{g*} - a_2^* + a_1^*)t^*$. Here, we choose a_1^* to be the velocity scale and the grid spacing Δx^* to be the length scale. Thus, the head of the expansion fan travels through one grid cell in each unit time interval. Starting from zero thickness, the expansion fan expands by $u_2^{g*}/a_1^* - a_2^*/a_1^* + 1 = 0.98$ grid cells in each unit time interval. Therefore, the spatial resolution of the expansion fan improves with time.
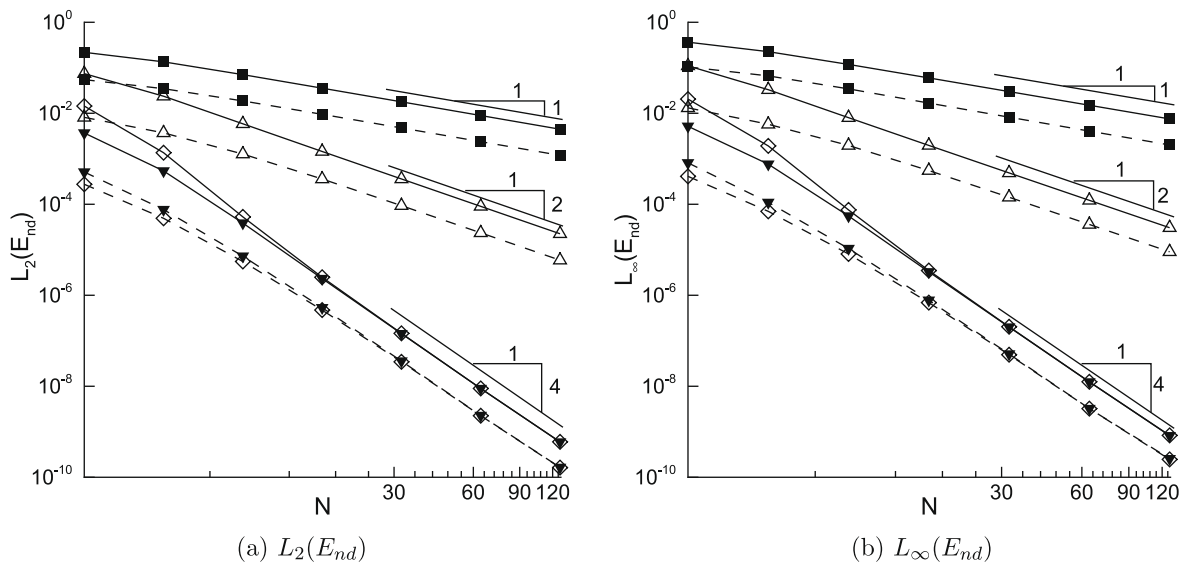
Fig. 11. Behavior of number-density error (E_{nd}) as a function of N for cases 2-1 and 2-3. Lines denote values of u_2 (solid lines: $u_2 = 1$; dashed lines: $u_2 = -0.4$). Symbols denote interpolation schemes (filled square: piecewise constant; unfilled delta: piecewise linear; unfilled diamond: natural cubic spline; filled gradient: Hermite).

The particles are assumed to be uniformly distributed in $x < 0$ at $t = 0$. The particles and the gas are initially stationary and are accelerated by the expansion fan. After the particles travel through the expansion fan and exit to the right of the tail end of the fan, they reach the post-expansion non-dimensional velocity of u_2^*/a_1^*. Like in the hyperbolic-tangent problem, the particles start from zero velocity and reach a final steady state again. Here we consider both tracer particles ($\tau^p = 0$) and inertial particles defined in terms of their non-dimensional time constant ($\tau^p = 3.89$). As discussed above, the approach to steady state is asymptotic for inertial particles. As a result, a relaxation zone exists behind the expansion fan.

In the results presented below, we used a uniform distribution of 5000 particles per cell ($n_{ppc} = 5000$) as an initial condition in the region to the left of the expansion wave. This large number of particles per cell provides a smooth representation of the continuous particle number-density field. Increasing the density of particles further did not change the results presented below. Although an "analytical solution" for the particle concentration field can be computed using the solution for the velocity field of a centered expansion fan, here we used the numerical results obtained with Hermite interpolation to define the "baseline solution" (or near-exact solution) from which the errors can be computed. The reason for this approximate approach is as follows.

At very early times, due to the poor resolution of the expansion wave the numerical solution for the gas velocity within the expansion fan deviates from the analytical solution. While the analytic solution presents discontinuities in the velocity gradient at both the head and tail of the expansion fan, these discontinuities are smoothed out in the numerical solution. These differences introduce deviations in the computed particle position from its exact position. But these systematic differences in the particle position do not contribute to grid-to-grid particle number-density fluctuation and therefore are not the focus of the current discussion.

To isolate interpolation-induced fluctuations in the particle number-density, here we extract the baseline solution from the Hermite-interpolation solution. This solution is taken to be a superposition of the baseline solution plus a fluctuating component. A eighth-order compact spatial filter is used to extract the baseline portion, which then can be subtracted from the different interpolated results to obtain the respective errors. Here, it should be pointed out that unlike in the previous examples, the carrier-phase velocity is computed numerically at the grid points and therefore the derivatives at the grid points for Hermite interpolation must be evaluated numerically. To maintain the higher-order accuracy of interpolation we employ a fifth-order compact scheme to compute the first derivatives at the grid points.

The number of particles per cell n_{ppc} thus obtained from the filtered Hermite solution for the present case is shown in Fig. 14(a). The non-dimensional time is $t = 136.1$ and accordingly the expansion fan at this time spreads over 134.1 grid points. The results for both the tracer and inertial particles are quite similar. It can be seen that n_{ppc} decreases from its initial value of 5000 per cell to around 2000 per cell to the right of the fan.

Fig. 15 shows the number-density error at $t = 136.1$. At this time, the head and tail of the expansion fan are located at $x = -136.1$ and -1.98, respectively. Also, the location of the tracer particle that initially was at the origin is now located at $x = 110.69$; this particle represents the particle contact surface. Note that particles that are immediately behind the particle contact passed through the expansion fan when it was very narrow and resolved by very few grid points. As a result, the interpolation error for these particles is expected to be quite large. In Fig. 15(a) the tracer particles between the contact and the tail of the expansion fan (i.e., for $-1.98 \leqslant x \leqslant 110.69$) have passed through the expansion fan. Particles located between
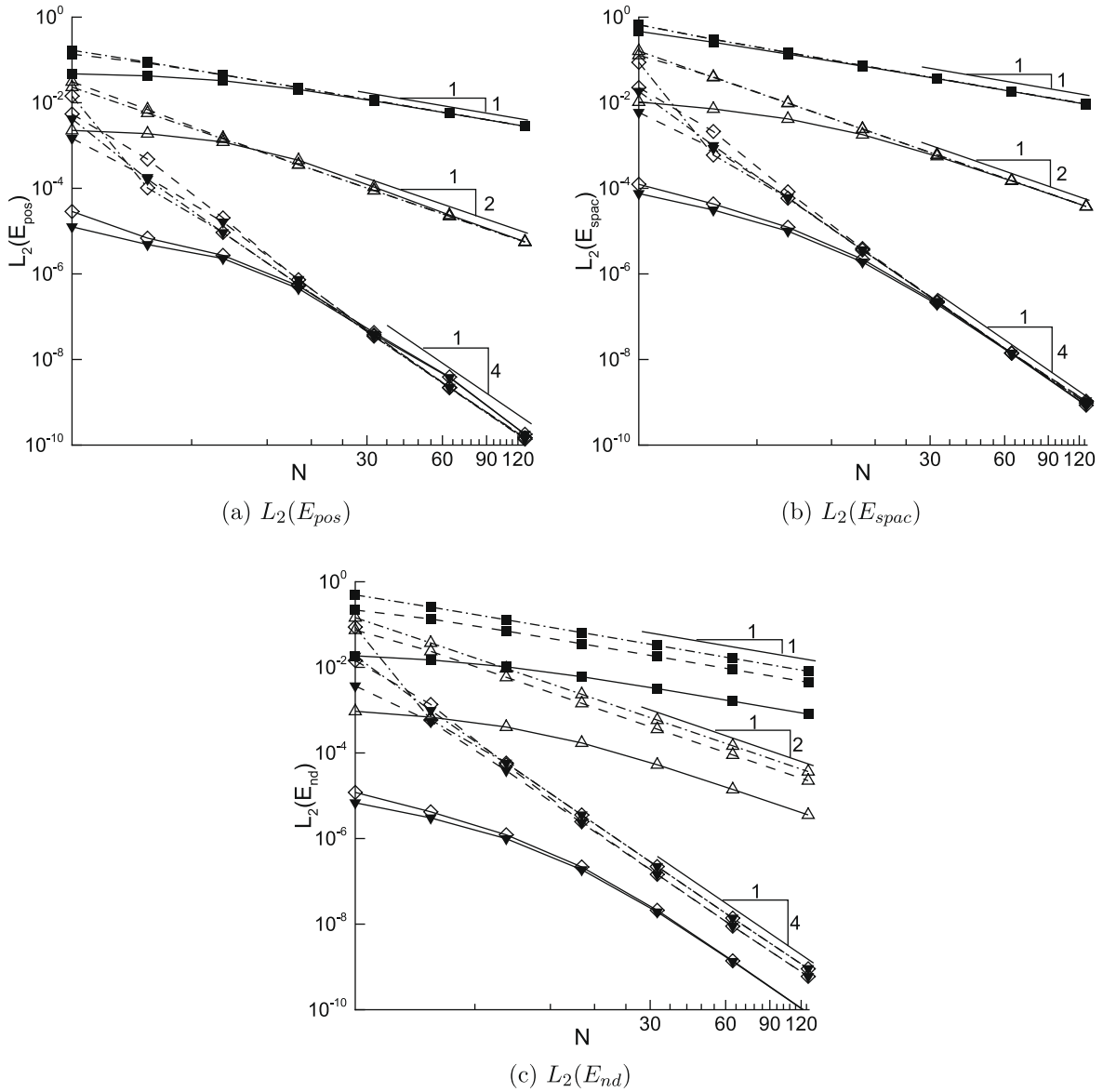
Fig. 12. Behavior of relative-position, spacing, and number-density errors ($E_{pos}, E_{spac}, E_{nd}$) as functions of N and u_2 for cases 2-1, 2-4, and 2-5. Lines denote values of u_2 (solid lines: $u_2 = 0.1$; dashed lines: $u_2 = 1$; dashed-dot lines: $u_2 = 10$). Symbols denote interpolation schemes (filled square: piecewise constant; unfilled delta: piecewise linear; unfilled diamond: natural cubic spline; filled gradient: Hermite).

$-136.1 \leqslant x \leqslant -1.98$ are still within the expansion fan, and particles to the left of the head of the fan remain unaffected. Fig. 14(b) presents the theoretical location x_h at which a particle enters the expansion fan and the thickness ξ_h of the expansion fan when the particle enters as a function of a particle's location at $t = 136.1$.

With the current non-dimensionalization, the thickness of the fan is equal to the number of grid points used to resolve it. It is expected that the expansion fan "seen" by a particle is thicker when the particle exits than when it enters. However, the largest number-density fluctuation is related to the smallest thickness of the expansion fan which a particle encounters. Therefore, one could choose the thickness of the expansion fan when a particle enters as the expansion fan thickness "seen" by the particle. Based on this thickness, the results for the hyperbolic-tangent profile presented in Fig. 10 can be used to estimate the number-density errors expected for the present problem of an unsteady expansion fan at $t = 136.1$. The estimates for the different interpolation methods are plotted as symbols in Fig. 15. The rapid decrease in the number-density error upstream of the particle contact observed in the numerical results is in excellent agreement with the estimates based on the frozen disturbance. The number-density error for the piecewise-constant interpolation is the largest and decays from about $O(1)$ close to the particle contact to about $O(10^{-2})$ in the expansion fan. The number-density errors for the piecewise linear and Hermite interpolations are orders of magnitude lower. Substantially higher errors are observed close to the particle con-
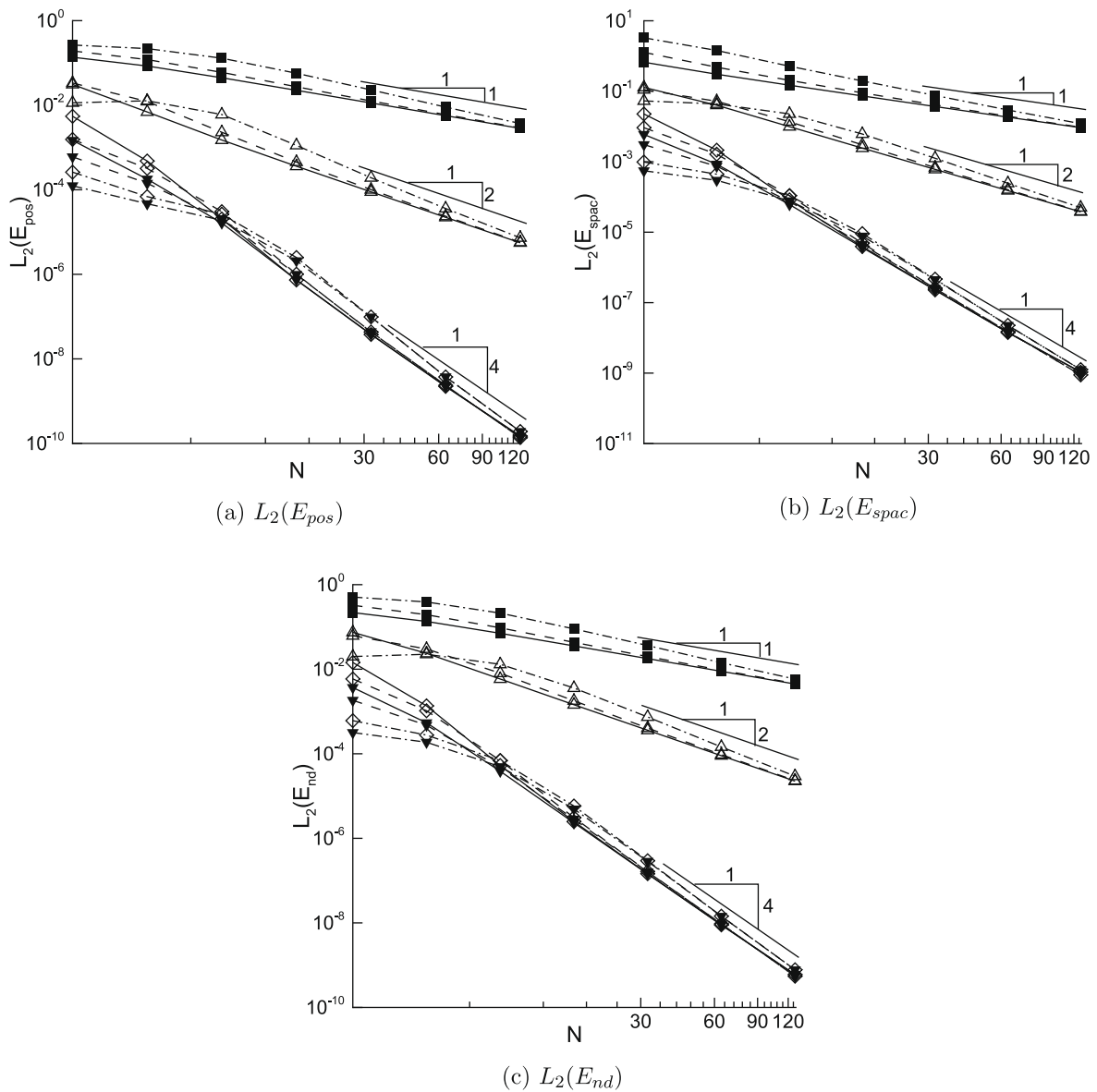
(a) $L_2(E_{pos})$

(b) $L_2(E_{spac})$

(c) $L_2(E_{nd})$

Fig. 13. Evolution of relative-position, spacing, and number-density errors ($E_{pos}, E_{spac}, E_{nd}$) as functions of N for cases 2-1, 2-6, and 2-7. Lines denote values of τ^p (solid lines: $\tau^p = 0$; dashed lines: $\tau^p = 1$; dashed-dot lines: $\tau^p = 10$). Symbols denote interpolation schemes (filled square: piecewise constant; unfilled delta: piecewise linear; unfilled diamond: natural cubic spline; filled gradient: Hermite).

tact for all interpolation methods. The results for inertial particles are quite similar to those for tracer particles. Thus particle inertia does not appear to greatly influence interpolation errors.

The above results were obtained with one-way coupling, where the gas flow is unaffected by the particles. To assess the influence of two-way coupling on number-density errors, we consider two cases with particle mass fractions of $Y^p = \{0.1, 0.5\}$. Numerical simulations were used to compute number-density errors in the same way as described above. The results are shown in Fig. 16. It is observed that the behavior of the number-density error with two-way coupling is qualitatively similar to that for one-way coupling.

A further observation can be made by comparing Figs. 15 and 16. It is seen that the number-density fluctuation wavelength changes with the mass fraction. When the mass fraction increases, the velocity jump across the expansion fan decreases, and therefore the number-density ratio across the expansion fan changes also. As shown in Section 5.2 and Fig. 9, the fluctuation wavelength depends on the numerator p if the number-density ratio can be written as p/q. For the present problem, as the mass loading increases, the number-density ratio $1/(1 + u_2^g)$ decreases, and the number-density fluctuation wavelength also decreases.
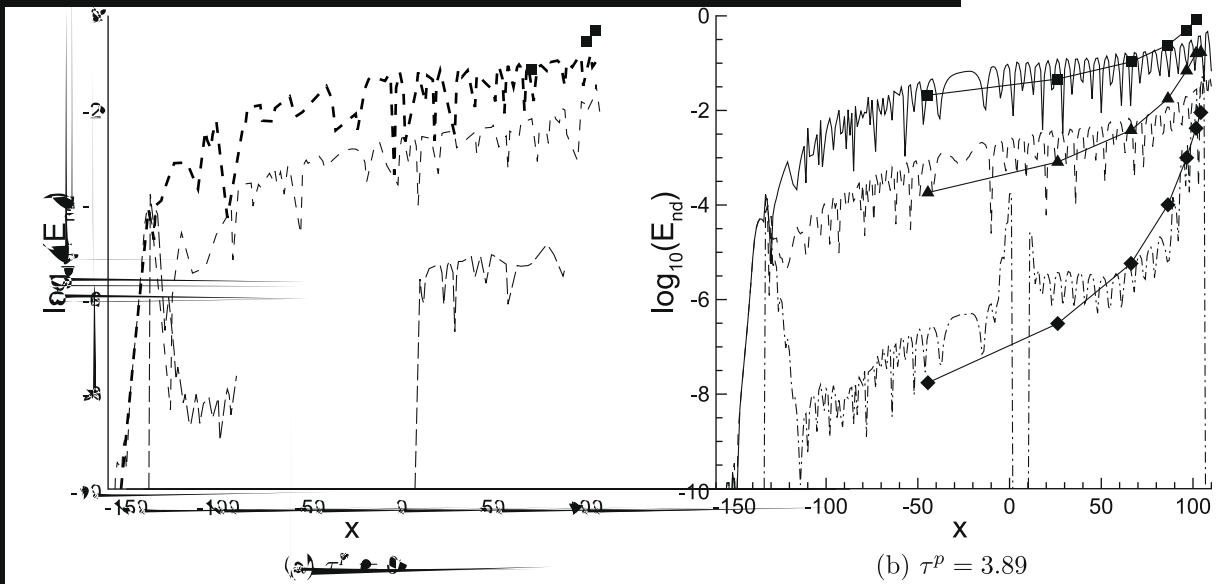
(b) $\tau^p = 3.89$

Fig. 15. Behavior of particle number-density error E_{nd} at $t = 136.1$ for a one-way coupled simulation of an expansion fan propagating into uniformly distributed particles. Solid lines with symbols denote error estimates for various interpolation schemes based on the analysis of the model problem with the hyperbolic-tangent profile (square: piecewise constant; delta: piecewise linear; diamond: Hermite). Lines without symbols denote the numerical results for various interpolation schemes (dashed line: piecewise constant; dashed-dot line: piecewise linear; long dashed lines: Hermite).

r shock wave propagating to
a problem leading to a shock
icles to the right of the shock
hock. For inertial particles, a
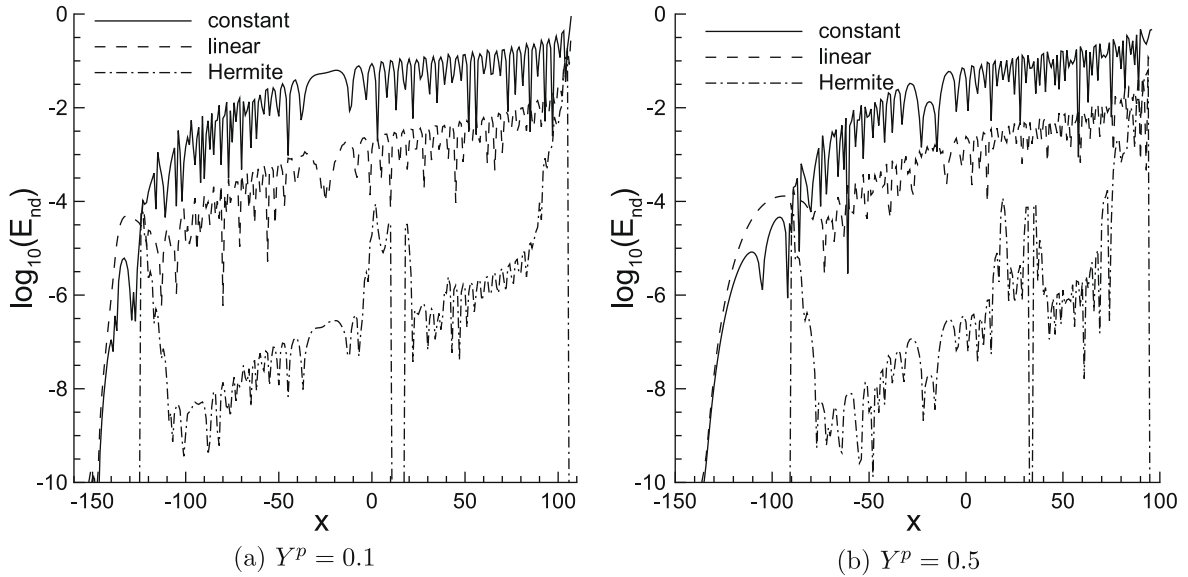value to the final post-shock

Fig. 16. Behavior of particle number-density error E_{nd} at $t = 136.1$ for a two-way coupled simulation of an expansion fan propagating into uniformly distributed particles as a function of the mass fraction Y^p.

The shock velocity can be obtained from the shock-wave Mach number,

$$M_s = \frac{u_s^*}{a_1^*} = \left(\frac{\gamma + 1}{2\gamma} \frac{p_2^*}{p_1^*} + \frac{\gamma - 1}{2\gamma} \right)^{1/2}, \tag{27}$$

where a_1^* is the speed of sound ahead of the shock. We take u_s^* to be the velocity scale and the grid spacing Δx^* to be the length scale. The non-dimensional post-shock gas velocity is then given by

$$u_2^g = \frac{u_2^{g*}}{u_s^*} = \frac{2}{\gamma + 1} \left(1 - \frac{1}{M_s^2} \right). \tag{28}$$

For the conditions considered here, the non-dimensional post-shock gas velocity is $u_2^g = 0.4$. As in the previous problem, the particles are initially uniformly distributed in the undisturbed region with $n_{ppc} = 5000$. After the passage of the shock, the number of particle per cell increases to $5000/(1 - u_2^g) = 8333$.

The number-density fluctuation amplitude is expected to be directly related to the number of grid points used to represent the shock. From the analysis of the model problem with the hyperbolic-tangent profile, it is anticipated that the number-density errors incurred by the various interpolation schemes are similar when the grid resolution is very poor (see Fig. 11). Therefore, we introduce extra viscosity in the present problem to artificially increase the shock thickness. The justification for doing so is discussed below. As shown in Fig. 17(a), the shock thickness is around 10 cells if measured by a similar approach used for the measuring the hyperbolic-tangent profile.

Similar to the problem of the expansion fan, the filtered Hermite interpolation results are used to define an "exact solution." The profiles of the number of particles per cell for the filtered Hermite solution for both tracer particles and inertial particles ($\tau^p = 6.25$) at the non-dimensional time $t = 130$ are shown in Fig. 17(b). Fig. 18 shows the number-density error plotted as a function of spatial location. With the current non-dimensionalization, the shock travels through one grid cell per unit time interval. The particle contact surface is located at $x = 51.6$ for the tracer particles and $x = 47.9$ for the inertial particles. Once the particles completely exit the shock wave, the number-density fluctuation is maintained at the same level (see the region $50 \leqslant x \leqslant 125$ in Fig. 18(a) and the region $50 \leqslant x \leqslant 90$ in Fig. 18(b)), and do not decay away from the particle contact as in the expansion fan. Where the particles have completely crossed the relaxation zone, the number-density fluctuation wavelength is exactly three cells. Because the number-density ratio across the shock is $1 - u_2 = 3/5$, and the number-density fluctuation wavelength is determined by the numerator, the computed number-density error fluctuation profile agrees with the theory.

The number-density error for both 5000 initial particles per grid cell and 1000 initial particles per cell are shown. The result is clearly invariant and does not exhibit one over square root decay. This establishes the independence of the interpolation-induced number-density fluctuation from the mean number-density. Based on the estimated shock thickness of 10, the results of the hyperbolic-tangent profile presented in Fig. 10 can be used to estimate the number-density errors for the present problem. This estimate is also shown in Fig. 18 and the agreement is quite good. Therefore, it is seen that
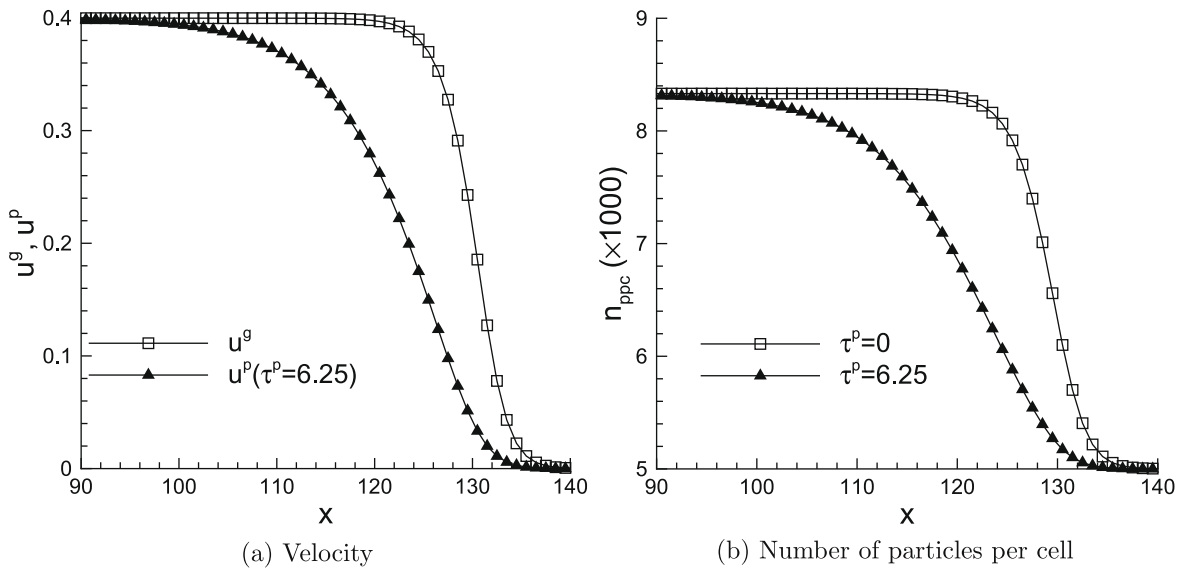
Fig. 17. Velocity and number of particle per cell profiles as functions of spatial location at time $t = 130$. The results shown here is from the filtered one-way coupled Hermite solution.
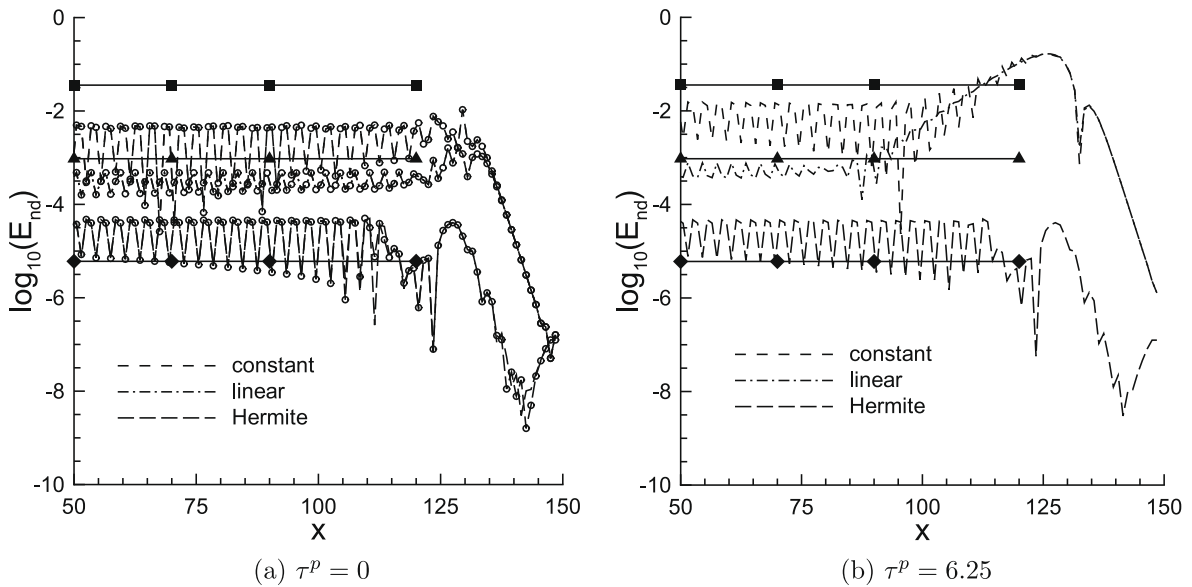

Fig. 18. Behavior of number-density error E_{nd} at $t = 130$ for a one-way coupled simulation of a shock wave propagating into uniformly distributed particles. Solid lines with filled symbols denote error estimates for various interpolation schemes based on the analysis of the model problem with the hyperbolic-tangent profile (square: piecewise constant; delta: piecewise linear; diamond: Hermite). Lines without symbols and with unfilled circle symbols denote numerical results. The lines without symbols denote the results with 5000 initial particles per cell; while those with unfilled circle symbols are for 1000 initial particles per cell. The line patterns are used to distinguish different interpolation schemes (dashed line: piecewise constant; dashed-dot line: piecewise linear; long dashed lines: Hermite interpolation).

even for different grid resolution, the simple analysis of the hyperbolic-tangent profile can be used to estimate the number-density fluctuation amplitude encountered in real computations.

The advantage of higher-order interpolation schemes is again noticeable in Fig. 18. The number-density error for the piecewise-constant interpolation is the largest at about $O(10^{-2})$. Linear interpolation gives errors more than one order of magnitude lower at about $O(10^{-3})$, while Hermite interpolation yields the smallest error at about $O(10^{-5})$. If the resolution used to resolve the shock is much smaller, for example if the dimensionless shock thickness is two, the errors from the interpolation schemes are of approximately the same order of magnitude. This is not surprising, as it is well-known that

higher-order methods can perform worse than lower-order methods when the grid resolution is poor. In complex three-dimensional simulations, it is unlikely that one can afford to resolve a shock wave with ten or more grid points. This is likely to pose problems in a one-way coupled simulation, as the shock generally tends to remain thin. However, if the particle mass fraction is not small, so that two-way coupled simulations are required, a finite-size relaxation zone exists behind the shock wave. The relaxation zone, together with the actual shock wave, can be viewed as a thickened "multiphase shock." Using ten or more points to resolve the relaxation zone is absolutely practical.

Finally, it should be reminded that the results shown in Sections 5.3 and 5.4 are independent of the number of particles used in the computation, namely the number-density fluctuation observed here will not decrease if one increases the number of particles. This can be confirmed by Fig. 18(a), where results with different particle number are shown. The lines without symbols denote the cases in which the initial number of particle per cell is 5000; while the lines with unfilled circle symbols denote the case with half number of particles. It can be seen that these two sets of lines almost perfectly overlap with each other. It also shows that the number of particles used here is large enough to screen out the influence of computational particle number. This also means that, the other two commonly known sources of number-density fluctuation have been perfectly excluded.

6. Conclusions

The present study explores a source of particle number-density, or concentration fluctuations in Eulerian–Lagrangian simulations of multiphase flows. The conventional understanding of number-density fluctuations is that they are generated by Lagrangian discretization (i.e., because of a limited number of particles). Therefore, increasing the number of particles is usually viewed as sufficient to limit the fluctuation amplitudes. We have found that another source of particle number-density fluctuation exists that is not related to Lagrangian discretization. This error source is fundamentally different because the fluctuations cannot be reduced by increasing the number of particles. As shown in this article through a sequence of problems, this type of fluctuation is caused by the error in the interpolation of the fluid velocity to the particle location.

The crucial point is that when a frozen fluid-velocity variation propagates through a fixed grid, the interpolant of the fluid-velocity variation changes not only in space but also in time. In other words, even if the exact fluid velocity is known at the grid points, the interpolated approximation to the fluid-velocity variation will change over time in a periodic manner (see Fig. 2). As a consequence, when the fluid-velocity variation propagates through the fixed grid, the time history of fluid velocity seen by a particle will depend on its location with respect to the grid, affecting its motion and final position. Thus the interpolation error generates a subgrid variation in the particle position after the passage of the fluid-velocity perturbation.

Note that in an actual simulation where the fluid flow is also numerically computed there will be Eulerian discretization error in the fluid velocity evaluated at the grid points. This error in the computed fluid velocity will contribute to an error in particle position and number-density. But as shown here an error in interpolating the fluid velocity to off-grid locations will lead to a special kind of number-density error, which can be substantial and subgrid in nature. In other words, an initially uniformly spaced particle distribution between two grid points, after the passage of the fluid-velocity perturbation, will be non-uniformly distributed with large variation in the inter-particle spacing. If either the fluid velocity has non-zero divergence or the particles have non-zero inertia, the particle distribution can undergo preferential accumulation. In which case the interpolation-induced subgrid fluctuations can manifest as grid-to-grid fluctuations. Note that here we have focused on the spatial (grid-to-grid) nature of the number-density fluctuation. Instead if one considers measurement over time as observed by a fixed probe, the spatial fluctuation will result in a corresponding spurious temporal fluctuation in the measured particle number-density. The short spatial wavelength of the fluctuation will translate to a high frequency noise in the measured number-density. These fluctuations are generally small, which may explain why they have not been noticed so far.

However, there exists some situations in which the fluctuations can become large and therefore must be dealt with. The case of an expansion fan propagating in a particle-laden fluid considered in Section 5.3 is a good example. In that case, all the interpolation methods tested here introduce significant number-density fluctuations for the particles that were accelerated by the expansion fan at early times when the fan was very thin. Therefore, this source of number-density fluctuations may not be negligible in compressible multiphase flow in which thin waves exist. The basic nature of this source of error is not, however, dependent on compressibility, and thus large errors can in principle be encountered in incompressible flows also.

This study employed two model problems with imposed fluid-velocity profiles to show how the number-density fluctuations are generated by the interpolation of the fluid velocity to the particle location. Different types of error have been plotted as a function of the grid resolution, with the goal of serving as guidelines for choosing the grid resolution for a given error level. Two physical problems in which the fluid velocity was obtained from numerical solutions of the Euler equations, namely of an expansion and a shock wave, were also considered. The number-density fluctuations observed in those computations match the results from the model problem. In general, higher-order interpolation methods, such as Hermite interpolation, result in reduced number-density fluctuations compared to lower-order schemes. Finally, it must be pointed out the several simplifications have been made in the present study. For example, we have used only one-dimensional examples with particle motion influenced by only the Stokes drag. However, the phenomenon described here will be valid in more complex 3D time-dependent flows that use more accurate drag and lift forces for particle motion. We hope the present study will help better explain (at least qualitatively) number-density fluctuations seen in such complex flows.

Acknowledgments

References

[1] S. Balachandar, M.R. Maxey, Methods for evaluating fluid velocities in spectral simulations of turbulence, J. Comput. Phys. 83 (1989) 96–125.
[2] M. Boivin, O. Simonin, K.D. Squires, Direct numerical simulation of turbulence modulation by particles in isotropic turbulence, J. Fluid Mech. 375 (1998) 235–263.
[3] J. Chao, A. Haselbacher, S. Balachandar, A massively parallel multi-block hybrid compact-WENO scheme for compressible flows, J. Comput. Phys. 228 (2009) 7473–7491.
[4] C.T. Crowe, Numerical-models for dilute gas-particle flows – review, J. Fluid Eng. 104 (1982) 297–303.
[5] M.W. Evans, F.H. Harlow, E. Bromberg, The particle-in-cell method for hydrodynamic calculations, Los Alamos National Lab NM, 1957.
[6] F.N. Fritsch, R.E. Carlson, Monotone piecewise cubic interpolation, SIAM J. Numer. Anal. 17 (1980) 238–246.
[7] R. Garg, C. Narayanan, D. Lakehal, S. Subramaniam, Accurate numerical estimation of interphase momentum transfer in Lagrangian–Eulerian simulations of dispersed two-phase flows, Int. J. Multiphase Flow 33 (2007) 1337–1364.
[8] F.H. Harlow, PIC and its progeny, Comput. Phys. Commun. 48 (1988) 1–10.
[9] K.C. Kannenberg, I.D. Boyd, Strategies for efficient particle resolution in the direct simulation Monte Carlo method, J. Comput. Phys. 157 (2000) 727–745.
[10] Y. Ling, A. Haselbacher, S. Balachandar, Modeling and simulation of explosive dispersal of particles in a multiphase explosion, AIAA Paper 2009-1532, 2009a.
[11] Y. Ling, A. Haselbacher, S. Balachandar, Transient phenomena in one-dimensional compressible gas-particle flows, Shock Waves 19 (2009) 67–81.
[12] F. Mashayek, F.A. Jaberi, Particle dispersion in forced isotropic low-Mach-number turbulence, Int. J. Heat Mass Transfer 42 (1999) 2823–2836.
[13] S.B. Pope, Particle method for turbulent flows: integration of stochastic model equations, J. Comput. Phys. 117 (1995) 332–349.
[14] G. Rudinger, Some properties of shock relaxation in gas flows carrying small particles, Phys. Fluids 7 (1964) 658–663.
[15] D.M. Snider, An compressible three-dimensional multiphase particle-in-cell model for dense particle flows, J. Comput. Phys. 170 (2001) 523–549.
[16] D.M. Snider, P.J. O'Rourke, M.J. Andrews, Sediment flow in inclined vessels calculated using a multiphase particle-in-cell model for dense particle flows, Int. J. Multiphase Flow 24 (1998) 1359–1382.
[17] K.D. Squires, J.K. Eaton, Particle response and turbulence modification in isotropic turbulence, Phys. Fluids 2 (1990) 1191–1203.
[18] S. Subramaniam, Statistical representation of a spray as a point process, Phys. Fluids 12 (2000) 2413–2431.
[19] S. Sundaram, L.R. Collins, Numerical considerations in simulating a turbulent suspension of finite-volume particles, J. Comput. Phys. 124 (1996) 337–350.
[20] P. Vedula, P.K. Yeung, Similarity scaling of acceleration and pressure statistics in numerical simulations of isotropic turbulence, Phys. Fluids 11 (1999) 1208–1220.
[21] A.A. Verevkin, Y.M. Tsirkunov, Flow of a dispersed phase in the Laval nozzle and in the test section of a two-phase hypersonic shock tunnel, J. Appl. Mech. Tech. Phys. 49 (2008) 198–789.
[22] J. Xu, S.B. Pope, Assessment of numerical accuracy of pdf Monte Carlo methods for turbulent reacting flows, J. Comput. Phys. 152 (1999) 192–230.